

Subband structure of a cylindrical HgTe nanowire: transition from normal type to inverted type

Rui Li (李睿) ^{1,*}

¹*Hebei Key Laboratory of Microstructural Material Physics,
School of Science, Yanshan University, Qinhuangdao 066004, China*

(Dated: December 23, 2024)

Based on the 6×6 Kane model in the spherical approximation, both the electron and the hole subband dispersions in a cylindrical HgTe nanowire are calculated using analytical method. The transcendental equations determining the subband energies in the nanowire are analytically derived by utilizing both the total angular momentum conservation and the hard wall boundary condition. We show there exists topological band transition in the HgTe nanowire, very similar to that demonstrated in a HgTe quantum well. Via tuning the radius of the nanowire, we find there is a gap-closing-and-reopening transition in the subband structure. When the radius is larger than the critical radius $R_c \approx 3.2185$ nm, the HgTe nanowire is in the inverted regime.

I. INTRODUCTION

Topological insulator is a new state of matter that has a bulk band gap similar to an ordinary insulator and at the same time has conducting states on its edge or surface [1–4]. Haldane’s model for realizing the quantum Hall effect in the absence of magnetic field was regarded as a model of the Chern insulator [5], where the topological invariant is called the Thouless-Kohmoto-Nightingale-Nijs number or the Chern number [6]. There is no time reversal symmetry in Haldane’s model. Later, Kane and Mele generalized Haldane’s model to the case of including the spin degree of freedom [7, 8]. The Kane-Mele model can be regarded as two spin copies of the Haldane model, and is time reversal invariant. The topological invariant in this case is characterized by the Z_2 index [8].

In 2006, Bernevig, Hughes, and Zhang proposed to look for the topological insulator phase in a HgTe/CdTe quantum well [9]. HgTe is a material with a negative band gap, while CdTe has a positive band gap [10]. Via tuning the well width, the subband structure of the quantum well exhibits gap-closing-and-reopening transition. When the well width is larger than a critical value, the quantum well is in a topological insulator phase with a pair of helical edge states [3, 9, 11]. This theoretical prediction was confirmed immediately by experiments [12]. Similar band inversion transition was proposed to exist in a InAs/GaSb/AlSb quantum well [13]. This topological band inversion transition is robust even in the presence of bulk inversion asymmetry [14–16].

It is an interesting question whether this topological band inversion transition still survive in a HgTe nanowire. Although a quasi-one-dimensional nanowire is geometrically different from a quasi-two-dimensional quantum well, it is highly likely both systems share the same kind of topological band inversion transition. After all, the negative band gap of the HgTe material seems

TABLE I. Bulk band parameters of the HgTe material [21, 22].

$\frac{\hbar^2 \epsilon_n}{2m_0}$ ^a	$\frac{\hbar^2 P^2}{2m_0}$	γ_1	γ_2	γ_3	$\gamma_s = \frac{2\gamma_2 + 3\gamma_3}{5}$
-0.303 eV	18.8 eV	4.1	0.5	1.3	0.98

^a m_0 is the free electron mass

to be the only essential factor in this topological transition [9]. Here we seek this topological band transition in a cylindrical HgTe nanowire. Also, for simplicity, we replace the barrier material CdTe with the vacuum, i.e., the HgTe nanowire is surrounded by a trivial insulator with an infinite band gap.

Following the method introduced by Sercel and Vahala [17], we rewrite the 6×6 Kane model [18], i.e., the $\mathbf{k} \cdot \mathbf{p}$ model involving both the Γ_6 and the Γ_8 bands, in the cylindrical coordinate representation. Both the bulk spectrum and bulk wave functions are obtained in this representation. The transcendental equations determining the subband dispersions are obtainable in terms of the bulk solutions. Especially, the transcendental equations at $k_z R = 0$ are explicitly given and discussed. Clear evidence of the band inversion transition, i.e., the gap-closing-and-reopening transition, at a critical nanowire radius is given. Also, the complete subband dispersions near this critical radius are calculated. We emphasize that in our calculations, we have used the spherical approximation in the Γ_8 band of the Kane model [19, 20].

II. KANE MODEL IN THE CYLINDRICAL COORDINATE REPRESENTATION

Semiconductor HgTe was known to have a negative band gap, i.e., the Γ_6 band of HgTe lies below its Γ_8 band [10]. It follows that the minimal bulk model of HgTe should be a 6×6 Kane model, that contains the information of the Γ_6 band, the Γ_8 band, and the coupling between them [18]. Previously, the subband structure of a HgTe/CdTe nanowire with a rectangular cross sec-

* rui.li@ysu.edu.cn

tion had been studied numerically, and the Rashba spin splitting was calculated as well [23]. Here we study analytically a cylindrical HgTe nanowire and focus on the tunability of the subband structure via the nanowire ra-

dius. We define the nanowire axis as the z axis, and the other two axes x and y are perpendicular to the nanowire. We employ the 6×6 Kane model in the spherical approximation in our study

$$H_0 = \frac{\hbar^2}{2m_0} \begin{pmatrix} \varepsilon_0 + \mathbf{k}^2 & 0 & -\frac{1}{\sqrt{2}}Pk_+ & \sqrt{\frac{2}{3}}Pk_z & \frac{1}{\sqrt{6}}Pk_- & 0 \\ 0 & \varepsilon_0 + \mathbf{k}^2 & 0 & -\frac{1}{\sqrt{6}}Pk_+ & \sqrt{\frac{2}{3}}Pk_z & \frac{1}{\sqrt{2}}Pk_- \\ -\frac{1}{\sqrt{2}}Pk_- & 0 & H_0^{33} & 2\sqrt{3}\gamma_s k_z k_- & \sqrt{3}\gamma_s k_-^2 & 0 \\ \sqrt{\frac{2}{3}}Pk_z & -\frac{1}{\sqrt{6}}Pk_- & 2\sqrt{3}\gamma_s k_z k_+ & H_0^{44} & 0 & \sqrt{3}\gamma_s k_-^2 \\ \frac{1}{\sqrt{6}}Pk_+ & \sqrt{\frac{2}{3}}Pk_z & \sqrt{3}\gamma_s k_+^2 & 0 & H_0^{55} & -2\sqrt{3}\gamma_s k_z k_- \\ 0 & \frac{1}{\sqrt{2}}Pk_+ & 0 & \sqrt{3}\gamma_s k_+^2 & -2\sqrt{3}\gamma_s k_z k_+ & H_0^{66} \end{pmatrix}, \quad (1)$$

where

$$\begin{aligned} H_0^{33} &= H_0^{66} = -[(\gamma_1 + \gamma_s)(k_x^2 + k_y^2) + (\gamma_1 - 2\gamma_s)k_z^2], \\ H_0^{44} &= H_0^{55} = -[(\gamma_1 - \gamma_s)(k_x^2 + k_y^2) + (\gamma_1 + 2\gamma_s)k_z^2] \end{aligned} \quad (2)$$

Here ε_0 , P , γ_1 , and γ_s are the bulk band parameters of the HgTe material (their values are given in Tab. I [21, 22]). Generally speaking, the Luttinger parameters γ_2 and γ_3 in the Γ_8 band are not equal. However, the spherical approximation (replacing $\gamma_{2,3}$ with γ_s) in most cases does not change the qualitative properties of a given system [24]. In particular, the amount of calculations including both the analytical and the numerical are greatly reduced by the spherical approximation. Considering the complexity of the size quantization of a nanowire involving the 6×6 bulk Hamiltonian, here we adopt the spherical approximation where the new parameter γ_s is set to $\gamma_s = (2\gamma_2 + 3\gamma_3)/5$ [25, 26].

The advantage of taking the spherical approximation can be seen right away. The bulk Hamiltonian H_0 now commutes with the z -component of the total angular

momentum F_z [17], where

$$F_z = -i\partial_\varphi + \begin{pmatrix} s_z & 0_{2 \times 4} \\ 0_{4 \times 2} & J_z \end{pmatrix}, \quad (3)$$

with s_z and J_z being the z -components of the standard spin-1/2 (for electron) and spin-3/2 (for hole) operators, respectively. Note that here we have chosen to study in a cylindrical coordinate representation where $x = r \cos \varphi$, $y = r \sin \varphi$, and $z = z$. The conservation of F_z indicates the Hilbert space of H_0 can be divided into a series of subspace. The Hilbert subspace specified with a general value of $F_z = m + 1/2$ ($m = 0, \pm 1, \pm 2, \dots$) is spanned by $J_m(\mu r)e^{im\varphi}|1/2\rangle_e$, $J_{m+1}(\mu r)e^{i(m+1)\varphi}|-1/2\rangle_e$, $J_{m-1}(\mu r)e^{i(m-1)\varphi}|3/2\rangle_h$, $J_m(\mu r)e^{im\varphi}|1/2\rangle_h$, $J_{m+1}(\mu r)e^{i(m+1)\varphi}|-1/2\rangle_h$, and $J_{m+2}(\mu r)e^{i(m+2)\varphi}|-3/2\rangle_h$. This Hilbert subspace has a dimension of six, such that we can rewrite H_0 as a 6×6 matrix in this Hilbert subspace. After some tedious derivations similar to that in Refs. [17, 27], we have

$$H_0 = \frac{\hbar^2}{2m_0} \begin{pmatrix} \varepsilon_0 + \mu^2 + k_z^2 & 0 & -\frac{i}{\sqrt{2}}P\mu & \sqrt{\frac{2}{3}}Pk_z & -\frac{i}{\sqrt{6}}P\mu & 0 \\ 0 & \varepsilon_0 + \mu^2 + k_z^2 & 0 & -\frac{i}{\sqrt{6}}P\mu & \sqrt{\frac{2}{3}}Pk_z & -\frac{i}{\sqrt{2}}P\mu \\ \frac{i}{\sqrt{2}}P\mu & 0 & H_0^{33} & -2\sqrt{3}i\gamma_s k_z \mu & -\sqrt{3}\gamma_s \mu^2 & 0 \\ \sqrt{\frac{2}{3}}Pk_z & \frac{i}{\sqrt{6}}P\mu & 2\sqrt{3}i\gamma_s k_z \mu & H_0^{44} & 0 & -\sqrt{3}\gamma_s \mu^2 \\ \frac{i}{\sqrt{6}}P\mu & \sqrt{\frac{2}{3}}Pk_z & -\sqrt{3}\gamma_s \mu^2 & 0 & H_0^{55} & 2\sqrt{3}i\gamma_s k_z \mu \\ 0 & \frac{i}{\sqrt{2}}P\mu & 0 & -\sqrt{3}\gamma_s \mu^2 & -2\sqrt{3}i\gamma_s k_z \mu & H_0^{66} \end{pmatrix}, \quad (4)$$

where H_0^{33} , H_0^{44} , H_0^{55} , and H_0^{66} have the same forms as that given by Eq. (2) in which a simple replacement $k_x^2 + k_y^2 = \mu^2$ should be made.

Diagonalizing the bulk Hamiltonian (4) in the cylindri-

cal coordinate representation, we obtain three branches

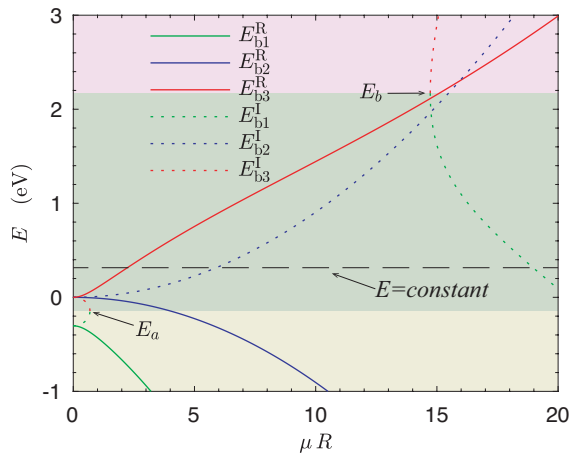


FIG. 1. The bulk band dispersions of HgTe at a fixed longitudinal wave vector $k_z R = 0$. The energies of the two touching points between the E_{b1}^I and E_{b3}^I branches are denoted by E_a and E_b , respectively. Here the nanowire radius is chosen as $R = 3$ nm. We divide the whole energy region into three subregions $E < E_a$, $E_a < E < E_b$, and $E_b < E$.

of bulk dispersions

$$\begin{aligned} E_{b1}^R &= \frac{\varepsilon_0}{2} - \frac{1}{2}(\gamma_1 + 2\gamma_s - 1)(\mu^2 + k_z^2) - \frac{1}{6}\chi\mu, \\ E_{b2}^R &= -(\gamma_1 - 2\gamma_s)(\mu^2 + k_z^2), \\ E_{b3}^R &= \frac{\varepsilon_0}{2} - \frac{1}{2}(\gamma_1 + 2\gamma_s - 1)(\mu^2 + k_z^2) + \frac{1}{6}\chi\mu, \end{aligned} \quad (5)$$

where

$$\begin{aligned} \chi\mu &= \left[12(\mu^2 + k_z^2) \left(3(\varepsilon_0 + \mu^2 + k_z^2)(\gamma_1 + 2\gamma_s) + 2P^2 \right) \right. \\ &\quad \left. + 9 \left(\varepsilon_0 - (\gamma_1 + 2\gamma_s - 1)(\mu^2 + k_z^2) \right)^2 \right]^{1/2}. \end{aligned} \quad (6)$$

Each branch is two-fold degenerate, i.e., there exist two bulk wave functions for each bulk dispersion (for details see appendix A). Note that we have implicitly assumed μ to be real in the bulk dispersions given by Eq. (5). However, in order to solve the subband quantization problem under a transverse hard wall confining potential, we also need to consider Bessel functions with imaginary argument $i\mu r$ [28]. Replacing μ with $i\mu$ in Eq. (5), we have the bulk dispersions in terms of the Bessel functions with imaginary argument [29]

$$E_{b1,2,3}^I = E_{b1,2,3}^R \Big|_{\mu=i\mu}. \quad (7)$$

We now have the complete bulk dispersions governed by the bulk Hamiltonian (4). The complete bulk dispersions with the longitudinal wave vector fixed at $k_z R = 0$ and $k_z R = 1.5$ are shown in Figs. 1 and 2, respectively. One can find that a given constant energy line always intersects the bulk dispersions three times. This means we always can write the eigenfunction in the nanowire as a linear combination of six bulk wave functions. Each intersecting point gives rise to two bulk wave

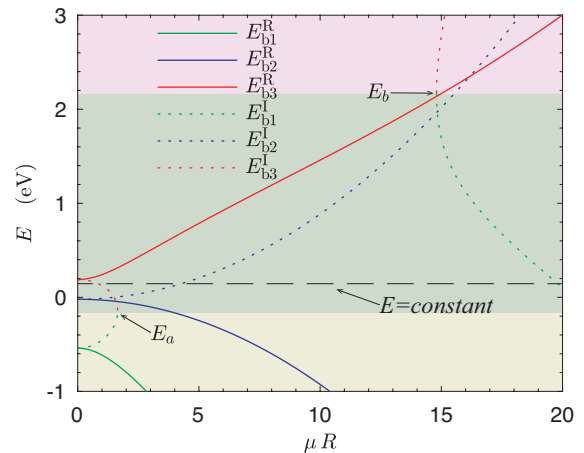


FIG. 2. The bulk band dispersions of HgTe at a fixed longitudinal wave vector $k_z R = 1.5$. The two energies E_a and E_b have the same meaning as that in Fig. 1, and the nanowire radius is $R = 3$ nm. We divide the whole energy region into three subregions $E < E_a$, $E_a < E < E_b$, and $E_b < E$.

functions, and three intersecting points correspond to six bulk wave functions. Also, from the bulk dispersions shown in Figs. 1 and 2, we find the whole energy region $-\infty < E < \infty$ can always be divided into three subregions, i.e., $E < E_a$, $E_a < E < E_b$, and $E_b < E$. The situation of intersecting between the constant energy line and the bulk dispersions varies with the subregion. Therefore, we need to select the proper bulk wave functions in each energy subregion.

III. SUBBAND ENERGIES AT $k_z R = 0$

Topological band inversion transition has been previously shown to occur in a HgTe quantum well where the CdTe material serves as the confining potential [9]. Here for simplicity, we consider a bare cylindrical HgTe nanowire, i.e., the vacuum serves as the confining potential. The vacuum can be considered as a trivial insulator with an infinite band gap. The Hamiltonian governing the subband quantization reads

$$H = H_0 + V(r), \quad (8)$$

where

$$V(r) = \begin{cases} 0_{6 \times 1}, & r < R, \\ \infty \begin{pmatrix} 1_{2 \times 1} \\ -1_{4 \times 1} \end{pmatrix}, & r > R, \end{cases} \quad (9)$$

with R being the nanowire radius. Here, we have a $+\infty$ confining potential for electron in the Γ_6 band and a $-\infty$ confining potential for hole in the Γ_8 band. In other words, we have a hard wall boundary condition both in the Γ_6 and Γ_8 bands. Also, recall that we are studying in a cylindrical coordinate representation where $x = r \cos \varphi$, $y = r \sin \varphi$, and $z = z$.

There is no confinement in the z direction, such that k_z is a conserved quantity in Hamiltonian (8). The energy eigenvalues of Hamiltonian (8) can always be written as a quasi-one-dimensional dispersion $E(k_z)$. Here we first focus on the subband energies at $k_z R = 0$. The bulk Hamiltonian (4) is block diagonalized when $k_z R = 0$, i.e., we can regroup the bulk Hamiltonian to a form with two nonvanishing 3×3 blocks. It is likely to have relatively simple results at this site. The block diagonalized feature of H_0 indicates we have two independent Hilbert subspaces, i.e., one subspace I spanned by $J_m(\mu r)e^{im\varphi}|1/2\rangle_e$, $J_{m-1}(\mu r)e^{i(m-1)\varphi}|3/2\rangle_h$, and $J_{m+1}(\mu r)e^{i(m+1)\varphi}|-1/2\rangle_h$, and the other subspace II spanned by $J_{m+1}(\mu r)e^{i(m+1)\varphi}|-1/2\rangle_e$, $J_m(\mu r)e^{im\varphi}|1/2\rangle_h$, and $J_{m+2}(\mu r)e^{i(m+2)\varphi}|-3/2\rangle_h$. Note that similar classification of the Hilbert subspaces has been used in studying the interface state between inverted and normal semiconductors [30]. In the following, we separately look for the subband energies in these two Hilbert subspaces.

Writing the eigenfunction as a linear combination of three bulk wave functions in each of the Hilbert subspaces, and imposing the hard wall boundary condition at $r = R$, we obtain one transcendental equation in the

Hilbert subspace I

$$\begin{vmatrix} M_{11}^{\pm} & M_{12}^{\pm} & 0 \\ \sqrt{3}J_{m-1}(\mu_1 R) & \sqrt{3}J_{m-1}(\mu_3 R) & -\frac{1}{\sqrt{3}}J_{m-1}(\mu_2 R) \\ J_{m+1}(\mu_1 R) & J_{m+1}(\mu_3 R) & J_{m+1}(\mu_2 R) \end{vmatrix} = 0, \quad (10)$$

and the other transcendental equation in the Hilbert subspace II

$$\begin{vmatrix} O_{11}^{\pm} & O_{12}^{\pm} & 0 \\ \frac{1}{\sqrt{3}}J_m(\mu_1 R) & \frac{1}{\sqrt{3}}J_m(\mu_3 R) & -\sqrt{3}J_m(\mu_2 R) \\ J_{m+2}(\mu_1 R) & J_{m+2}(\mu_3 R) & J_{m+2}(\mu_2 R) \end{vmatrix} = 0, \quad (11)$$

where

$$\begin{aligned} M_{11}^{\pm} &= -i \frac{3\varepsilon_0 + 3(\gamma_1 + 2\gamma_s + 1)\mu_1^2 \pm \chi_{\mu_1}}{\sqrt{6}P\mu_1} J_m(\mu_1 R), \\ M_{12}^{\pm} &= -i \frac{3\varepsilon_0 + 3(\gamma_1 + 2\gamma_s + 1)\mu_3^2 \pm \chi_{\mu_3}}{\sqrt{6}P\mu_3} J_m(\mu_3 R), \\ O_{11}^{\pm} &= -i \frac{3\varepsilon_0 + 3(\gamma_1 + 2\gamma_s + 1)\mu_1^2 \pm \chi_{\mu_1}}{3\sqrt{2}P\mu_1} J_{m+1}(\mu_1 R), \\ O_{12}^{\pm} &= -i \frac{3\varepsilon_0 + 3(\gamma_1 + 2\gamma_s + 1)\mu_3^2 \pm \chi_{\mu_3}}{3\sqrt{2}P\mu_3} J_{m+1}(\mu_3 R) \end{aligned} \quad (12)$$

and

$$\begin{aligned} \mu_{1/3} &= \frac{\left(\mp \sqrt{(3(\varepsilon_0 - E)(\gamma_1 + 2\gamma_s) + 3E + 2P^2)^2 - 36E(\varepsilon_0 - E)(\gamma_1 + 2\gamma_s) - 3\varepsilon_0(\gamma_1 + 2\gamma_s) + 3E(\gamma_1 + 2\gamma_s - 1) - 2P^2} \right)^{1/2}}{\sqrt{6(\gamma_1 + 2\gamma_s)}}, \\ \mu_2 &= \sqrt{\frac{-E}{\gamma_1 - 2\gamma_s}}. \end{aligned} \quad (13)$$

Here $\mu_{1,3}$ are solved from $E_{b1,3}$ and μ_2 is solved from E_{b2} (see Eq. (5)). Note that the subband energy E is the only unknown in Eqs. (10) and (11), and how to select the proper matrix elements M_{11}^{\pm} , M_{12}^{\pm} , O_{11}^{\pm} , and O_{12}^{\pm} will be explained in the following.

Let us discuss the special case $|F_z| = 1/2$. This case is important because the subband energies at the fundamental band gap are given by the smallest total angular momentum $|F_z| = 1/2$ [17, 26, 27, 29, 31, 32], i.e., $m = 0$ and $m = -1$. For the case $m = 0$, using the property of the Bessel function $J_{-1}(\mu_2 R) = -J_1(\mu_2 R)$ [28], the transcendental equation (10) can be further reduced to two independent transcendental equations

$$\begin{vmatrix} M_{11}^{\pm}|_{m=0} & M_{12}^{\pm}|_{m=0} \\ J_1(\mu_1 R) & J_1(\mu_3 R) \end{vmatrix} = 0, \quad \text{and} \quad J_1(\mu_2 R) = 0. \quad (14)$$

For the case $m = -1$, the transcendental equation (11) can be further reduced to two independent transenden-

tal equations

$$\begin{vmatrix} O_{11}^{\pm}|_{m=-1} & O_{12}^{\pm}|_{m=-1} \\ J_1(\mu_1 R) & J_1(\mu_3 R) \end{vmatrix} = 0, \quad \text{and} \quad J_1(\mu_2 R) = 0. \quad (15)$$

The above two equations (14) and (15) are very important for understanding the band inversion transition at a critical radius.

We now explain how to select the proper matrix elements in the transcendental equations (10) and (11). This selection is intimately relevant to the region division shown in Fig. 1. In energy subregion $E < E_a$, we should select the matrix elements M_{11}^- and M_{12}^- in Eq. (10), and O_{11}^- and O_{12}^- in Eq. (11). In energy subregion $E_a < E < E_b$, we should select the matrix elements M_{11}^+ and M_{12}^+ in Eq. (10), and O_{11}^+ and O_{12}^+ in Eq. (11). In energy subregion $E_b < E$, we should select the matrix elements M_{11}^+ and M_{12}^+ in Eq. (10), and O_{11}^+ and O_{12}^+ in Eq. (11).

Although we have derived the transcendental equations of the subband energy E at $k_z R = 0$ in the whole

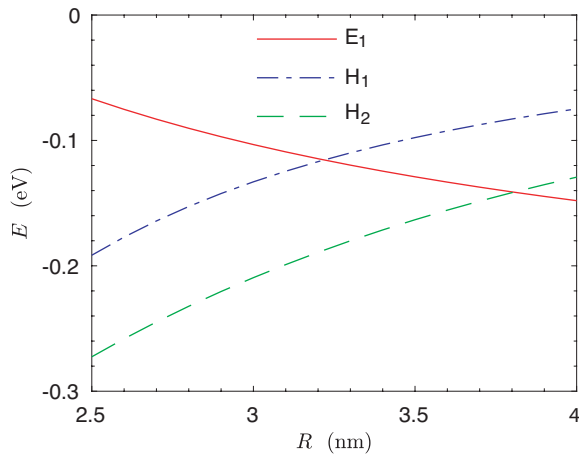


FIG. 3. The subband energies at $k_z R = 0$ as a function of the nanowire radius R . The lowest electron subband intersects with the two top most hole subbands both at $R \approx 3.2185$ nm and $R \approx 3.8056$ nm. The fundamental band gap closes at the critical radius $R_c \approx 3.2185$ nm.

energy region $-\infty < E < \infty$, the most interesting subband energies actually lie in the band gap region of the HgTe [9], i.e., -0.303 eV $< E < 0$ eV. Also, both the lowest electron subband and the top most hole subbands are given by the $|F_z| = 1/2$, i.e., $m = 0$ and $m = -1$. If we are only interested in the subband energies at the fundamental band gap, we just need to solve Eqs (14) and (15). The lowest electron subband and the two top most hole subbands as a function of the nanowire radius are shown in Fig. 3. We find the lowest electron subband intersects with the two top most hole subbands both at $R \approx 3.2185$ nm and $R \approx 3.8056$ nm. The radius $R \approx 3.2185$ nm can be regarded as the critical radius R_c , at which the fundamental band gap closes.

IV. SUBBAND DISPERSIONS

We now continue to study the subband energies at a general wave vector site $k_z R \neq 0$, i.e., we want to obtain the subband energies as a function of the longitudinal wave vector k_z . Similar to the case of $k_z R = 0$, here we still can derive a series of transcendental equations with respect to the region division of the energy. When $k_z R \neq 0$, from the bulk spectrum shown in Fig. 2, we find the whole energy region can still be divided into three subregions.

In energy subregion $E < E_a$, a constant energy line intersects the bulk dispersion E_{b1} two times and the bulk dispersion E_{b2} one time, such that the eigenfunction is expanded in terms of four bulk wave functions from the E_{b1} branch and two bulk wave functions from the E_{b2} branch. In energy subregion $E_a < E < E_b$, a constant energy line intersects each of the three bulk dispersions $E_{b1,2,3}$ just one time, such that the eigenfunction is expanded in terms of two bulk wave functions from the E_{b1}

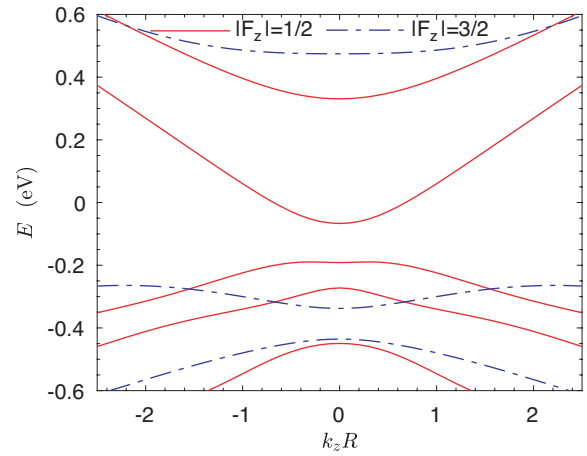


FIG. 4. Subband dispersions in a cylindrical HgTe nanowire with radius $R = 2.5$ nm. The electron subband E_1 lies above the hole subband H_1 . The nanowire is in the normal regime.

branch, two bulk wave functions from the E_{b2} branch, and two bulk wave functions from the E_{b3} branch. In energy subregion $E_b < E$, a constant energy line intersects the bulk dispersion E_{b3} two times and the bulk dispersion E_{b2} one time, such that the eigenfunction is expanded in terms of four bulk wave functions from the E_{b3} branch and two bulk wave functions from the E_{b2} branch. Let the eigenfunction vanish at the boundary $\Psi(R, \varphi, z) = 0$, we are able to obtain six equations of the expansion coefficients. Let the determinant of the coefficient matrix equal to zero, we have the transcendental equation in each of the three energy subregions.

Due to the tedious expression of the bulk wave functions (see appendix A), here we do not show these 6×6 coefficient matrices in the three energy subregions. The procedure of deriving these 6×6 coefficient matrices is exact the same as that in obtaining the hole subband dispersions in a Ge nanowire [27, 29]. Solving these three transcendental equations, we are able to have the complete subband dispersions $E(k_z)$. Certainly, our method is self-consistent. At the site $k_z R = 0$, these transcendental equations, i.e., equalling the determinant of the 6×6 coefficient matrices to zero, can be reduced to two independent transcendental equations given by Eqs. (10) and (11).

Since we have shown evidence of the band inversion transition at a critical radius via calculating the subband energies at $k_z R = 0$ in Sec. III, here we show the complete subband dispersions near this transition point. The subband dispersions in a cylindrical HgTe nanowire with radii $R = 2.5$ nm, $R = 3.2185$ nm, and $R = 3.4$ nm are shown in Figs. 4, 5, and 6, respectively. At the critical radius $R_c \approx 3.2185$ nm, the HgTe nanowire has a vanishing band gap (see Fig. 5). For radius $R < R_c$, the HgTe nanowire has a normal subband structure, i.e., the lowest E_1 subband lies above the top most H_1 subband (see Fig. 4). While for radius $R_c < R$, the HgTe nanowire has an inverted subband structure, i.e., the lowest E_1 sub-

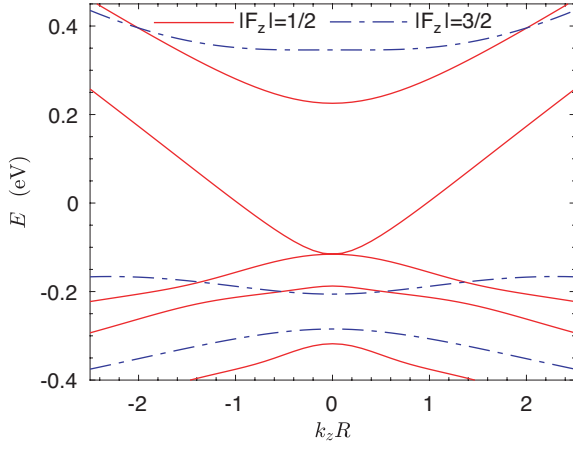


FIG. 5. Subband dispersions in a cylindrical HgTe nanowire with radius $R = 3.2185$ nm. The electron subband E_1 touches with the hole subband H_1 at $k_z R = 0$, the band gap vanishes. The nanowire is in the critical regime.

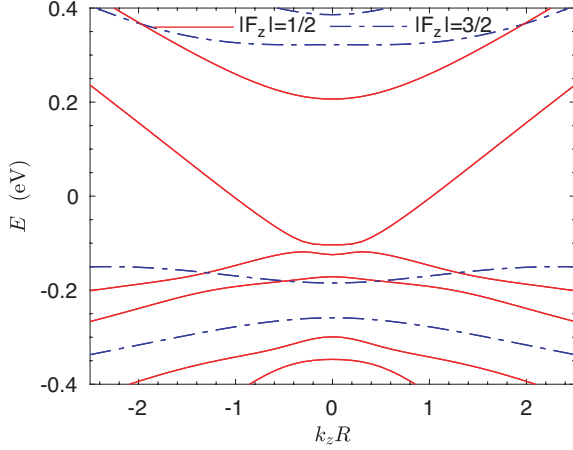


FIG. 6. Subband dispersions in a cylindrical HgTe nanowire with radius $R = 3.4$ nm. The electron subband E_1 lies below the hole subband H_1 , and the anticrossings between subbands E_1 and H_1 give rise to a band gap. The nanowire is in the inverted regime.

band lies below the top most H_1 subband (see Fig. 6). Now, the anticrossings between subbands E_1 and H_1 give rise to a band gap at $k_z R \neq 0$. Both the low-energy effective Hamiltonian of a HgTe nanowire with $R > R_c$ and whether there are edge states in this case will be studied in a separate paper.

V. SUMMARY

In summary, we have analytically solved the effective mass model of a cylindrical HgTe nanowire involving both the Γ_6 and Γ_8 bands. Both the spherical approximation and the hard-wall boundary condition are used in our calculations. A series of transcendental equations determining the subband energies are analytically derived.

Both the subband energies at $k_z R = 0$ and the complete subband dispersions are calculated and discussed. Topological band inversion transition is shown to occur at a critical radius. The HgTe nanowire has an inverted subband structure when its radius is larger than this critical radius.

Appendix A: Bulk wave functions

Diagonalizing the 6×6 bulk Hamiltonian (4) given in a cylindrical coordinate representation, we obtain six bulk wave functions. There are two bulk wave functions for each bulk dispersion shown in Eq. (5). The two bulk wave functions corresponding to the bulk dispersion E_{b1} are given by

$$\begin{pmatrix} \frac{\sqrt{2}k_z(3\varepsilon_0+3(\gamma_1+2\gamma_s+1)(\mu^2+k_z^2)-\chi\mu)}{3P\mu^2} J_m(\mu r) e^{im\varphi} \\ -i \frac{3\varepsilon_0+3(\gamma_1+2\gamma_s+1)(\mu^2+k_z^2)-\chi\mu}{3\sqrt{2}P\mu} J_{m+1}(\mu r) e^{i(m+1)\varphi} \\ \frac{2ik_z}{\mu} J_{m-1}(\mu r) e^{i(m-1)\varphi} \\ \frac{4k_z^2+\mu^2}{\sqrt{3}\mu^2} J_m(\mu r) e^{im\varphi} \\ 0 \\ J_{m+2}(\mu r) e^{i(m+2)\varphi} \end{pmatrix}, \quad (\text{A1})$$

and

$$\begin{pmatrix} -i \frac{3\varepsilon_0+3(\gamma_1+2\gamma_s+1)(\mu^2+k_z^2)-\chi\mu}{\sqrt{6}P\mu} J_m(\mu r) e^{im\varphi} \\ 0 \\ \sqrt{3} J_{m-1}(\mu r) e^{i(m-1)\varphi} \\ -\frac{2ik_z}{\mu} J_m(\mu r) e^{im\varphi} \\ J_{m+1}(\mu r) e^{i(m+1)\varphi} \\ 0 \end{pmatrix}. \quad (\text{A2})$$

The two bulk wave functions corresponding to the bulk dispersion E_{b2} are given by

$$\begin{pmatrix} 0 \\ 0 \\ \frac{2ik_z}{\mu} J_{m-1}(\mu r) e^{i(m-1)\varphi} \\ -\sqrt{3} J_m(\mu r) e^{im\varphi} \\ 0 \\ J_{m+2}(\mu r) e^{i(m+2)\varphi} \end{pmatrix}, \quad (\text{A3})$$

and

$$\begin{pmatrix} 0 \\ 0 \\ -\frac{4k_z^2+\mu^2}{\sqrt{3}\mu^2} J_{m-1}(\mu r) e^{i(m-1)\varphi} \\ -\frac{2ik_z}{\mu} J_m(\mu r) e^{im\varphi} \\ J_{m+1}(\mu r) e^{i(m+1)\varphi} \\ 0 \end{pmatrix}. \quad (\text{A4})$$

The two bulk wave functions corresponding to the bulk dispersion E_{b3} are given by

$$\begin{pmatrix} \frac{\sqrt{2}k_z(3\varepsilon_0+3(\gamma_1+2\gamma_s+1)(\mu^2+k_z^2)+\chi\mu)}{3P\mu^2} J_m(\mu r) e^{im\varphi} \\ -i \frac{3\varepsilon_0+3(\gamma_1+2\gamma_s+1)(\mu^2+k_z^2)+\chi\mu}{3\sqrt{2}P\mu} J_{m+1}(\mu r) e^{i(m+1)\varphi} \\ \frac{2ik_z}{\mu} J_{m-1}(\mu r) e^{i(m-1)\varphi} \\ \frac{4k_z^2+\mu^2}{\sqrt{3}\mu^2} J_m(\mu r) e^{im\varphi} \\ 0 \\ J_{m+2}(\mu r) e^{i(m+2)\varphi} \end{pmatrix}, \quad (\text{A5})$$

and

$$\begin{pmatrix} -i \frac{3\varepsilon_0+3(\gamma_1+2\gamma_s+1)(\mu^2+k_z^2)+\chi\mu}{\sqrt{6}P\mu} J_m(\mu r) e^{im\varphi} \\ 0 \\ \sqrt{3} J_{m-1}(\mu r) e^{i(m-1)\varphi} \\ -\frac{2ik_z}{\mu} J_m(\mu r) e^{im\varphi} \\ J_{m+1}(\mu r) e^{i(m+1)\varphi} \\ 0 \end{pmatrix}. \quad (\text{A6})$$

The eigenfunction of Hamiltonian (8) can be written as a linear combination of the above bulk wave functions.

-
- [1] M. Z. Hasan and C. L. Kane, Colloquium: Topological insulators, *Rev. Mod. Phys.* **82**, 3045 (2010).
- [2] X.-L. Qi and S.-C. Zhang, Topological insulators and superconductors, *Rev. Mod. Phys.* **83**, 1057 (2011).
- [3] B. A. Bernevig, *Topological insulators and topological superconductors* (Princeton university press, 2013).
- [4] S.-Q. Shen, *Topological insulators*, Vol. 174 (Springer, 2012).
- [5] F. D. M. Haldane, Model for a quantum hall effect without landau levels: Condensed-matter realization of the "parity anomaly", *Phys. Rev. Lett.* **61**, 2015 (1988).
- [6] D. J. Thouless, M. Kohmoto, M. P. Nightingale, and M. den Nijs, Quantized hall conductance in a two-dimensional periodic potential, *Phys. Rev. Lett.* **49**, 405 (1982).
- [7] C. L. Kane and E. J. Mele, Quantum spin hall effect in graphene, *Phys. Rev. Lett.* **95**, 226801 (2005).
- [8] C. L. Kane and E. J. Mele, Z_2 topological order and the quantum spin hall effect, *Phys. Rev. Lett.* **95**, 146802 (2005).
- [9] B. A. Bernevig, T. L. Hughes, and S.-C. Zhang, Quantum spin hall effect and topological phase transition in HgTe quantum wells, *Science* **314**, 1757 (2006).
- [10] O. Madelung, *Semiconductors: data handbook* (Springer Science & Business Media, 2004).
- [11] M. König, H. Buhmann, L. W. Molenkamp, T. Hughes, C.-X. Liu, X.-L. Qi, and S.-C. Zhang, The quantum spin hall effect: Theory and experiment, *Journal of the Physical Society of Japan* **77**, 031007 (2008).
- [12] M. König, S. Wiedmann, C. Brüne, A. Roth, H. Buhmann, L. W. Molenkamp, X.-L. Qi, and S.-C. Zhang, Quantum spin hall insulator state in HgTe quantum wells, *Science* **318**, 766 (2007).
- [13] C. Liu, T. L. Hughes, X.-L. Qi, K. Wang, and S.-C. Zhang, Quantum spin hall effect in inverted type-II semiconductors, *Phys. Rev. Lett.* **100**, 236601 (2008).
- [14] X. Dai, T. L. Hughes, X.-L. Qi, Z. Fang, and S.-C. Zhang, Helical edge and surface states in hgte quantum wells and bulk insulators, *Phys. Rev. B* **77**, 125319 (2008).
- [15] R. Winkler, L. Wang, Y. Lin, and C. Chu, Robust level coincidences in the subband structure of quasi-2D systems, *Solid State Communications* **152**, 2096 (2012).
- [16] S. A. Tarasenko, M. V. Durnev, M. O. Nestoklon, E. L. Ivchenko, J.-W. Luo, and A. Zunger, Split dirac cones in HgTe/CdTe quantum wells due to symmetry-enforced level anticrossing at interfaces, *Phys. Rev. B* **91**, 081302 (2015).
- [17] P. C. Sercel and K. J. Vahala, Analytical formalism for determining quantum-wire and quantum-dot band structure in the multiband envelope-function approximation, *Phys. Rev. B* **42**, 3690 (1990).
- [18] E. O. Kane, Band structure of indium antimonide, *Journal of Physics and Chemistry of Solids* **1**, 249 (1957).
- [19] J. M. Luttinger, Quantum theory of cyclotron resonance in semiconductors: General theory, *Phys. Rev.* **102**, 1030 (1956).
- [20] R. Winkler, *Spin-Orbit Coupling Effects in Two-Dimensional Electron and Hole Systems* (Springer, Berlin, 2003).
- [21] X. C. Zhang, A. Pfeuffer-Jeschke, K. Ortner, V. Hock, H. Buhmann, C. R. Becker, and G. Landwehr, Rashba splitting in n-type modulation-doped HgTe quantum wells with an inverted band structure, *Phys. Rev. B* **63**, 245305 (2001).
- [22] E. G. Novik, A. Pfeuffer-Jeschke, T. Jungwirth, V. Latussek, C. R. Becker, G. Landwehr, H. Buhmann, and L. W. Molenkamp, Band structure

- of semimagnetic $\text{Hg}_{1-y}\text{Mn}_y\text{Te}$ quantum wells, *Phys. Rev. B* **72**, 035321 (2005).
- [23] J. A. Budagosky, Cross-section geometry effects in the subband structure and spin-related properties of a HgTe/CdTe nanowire, *Phys. Rev. B* **96**, 115443 (2017).
- [24] R. Li and Z.-Q. Li, Low-energy hole subband dispersions in a cylindrical Ge nanowire: the effects of the nanowire growth direction, *Journal of Physics: Condensed Matter*, **35**, 345301 (2023).
- [25] A. Baldereschi and N. O. Lipari, Spherical model of shallow acceptor states in semiconductors, *Phys. Rev. B* **8**, 2697 (1973).
- [26] C. Kloeffel, M. Trif, and D. Loss, Strong spin-orbit interaction and helical hole states in Ge/Si nanowires, *Phys. Rev. B* **84**, 195314 (2011).
- [27] R. Li, Hole subband dispersions and strong ‘spin’-orbit coupling in a cylindrical Ge nanowire (2024), [arXiv:2411.16703 \[cond-mat.mes-hall\]](https://arxiv.org/abs/2411.16703).
- [28] Z. X. Wang and D. R. Guo, *Special Functions* (World Scientific, Singapore, 1989).
- [29] R. Li, Hole subband dispersions in a cylindrical Ge nanowire: exact results based on the axial Luttinger–Kohn Hamiltonian, *Journal of Physics: Condensed Matter*, **36**, 235301 (2024).
- [30] A. Khaetskii, V. Golovach, and A. Kiefer, Revisiting the physical origin and nature of surface states in inverted-band semiconductors, *Phys. Rev. B* **105**, 035305 (2022).
- [31] M. Sweeny, J. Xu, and M. Shur, Hole subbands in one-dimensional quantum well wires, *Superlattices and Microstructures* **4**, 623 (1988).
- [32] D. Csontos, P. Brusheim, U. Zülicke, and H. Q. Xu, Spin- $\frac{3}{2}$ physics of semiconductor hole nanowires: Valence-band mixing and tunable interplay between bulk-material and orbital bound-state spin splittings, *Phys. Rev. B* **79**, 155323 (2009).